FULL PAPER

Enhancing composition control of alloy nanoparticles from gas aggregation source by in operando optical emission spectroscopy

Jonas Drewes[1] | Alexander Vahl[1] | Niko Carstens[1] |
Thomas Strunskus[1] | Oleksandr Polonskyi[1,2] | Franz Faupel[1]

[1]Institute for Materials Science–Chair for Multicomponent Materials, Faculty of Engineering, Christian-Albrechts-University of Kiel, Kiel, Germany

[2]Department of Chemical Engineering, University of California–Santa Barbara, Santa Barbara, California, USA

Correspondence
Oleksandr Polonskyi, Department of Chemical Engineering, University of California–Santa Barbara, Engineering II, Santa Barbara, CA 93106-5080, USA.
Email: polonskyi.oleksandr@gmail.com

Franz Faupel, Institute for Materials Science–Chair for Multicomponent Materials, Faculty of Engineering, Christian-Albrechts-University of Kiel, Kaiserstraße 2, D-24143 Kiel, Germany.
Email: ff@tf.uni-kiel.de

Abstract

The use of multicomponent targets allows the gas-phase synthesis of a large variety of alloy nanoparticles (NPs) via gas aggregation sources. However, the redeposition of sputtered material impacts the composition of alloy NPs, as demonstrated here for the case of AgAu alloy NPs. To enable NPs with tailored Au fractions, in operando control over the composition of the NPs is in high demand. We suggest the use of optical emission spectroscopy as a versatile diagnostic tool to determine and control the composition of the NPs. A strong correlation between operating pressure, intensity ratio of Ag and Au emission lines, and the obtained NP compositions is observed. This allows precise in operando control of alloy NP composition obtained from multicomponent targets.
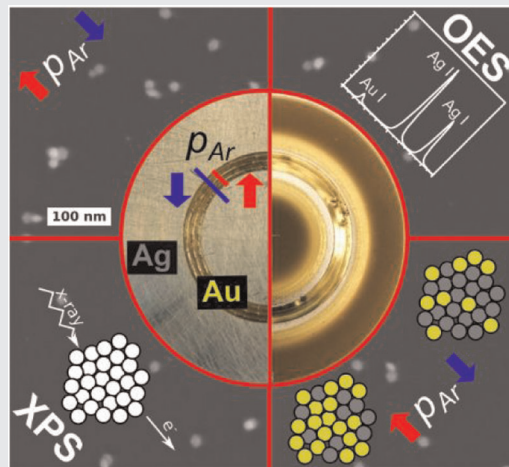
KEYWORDS

alloy nanoparticle, gas aggregation cluster source, gas-phase synthesis, in operando optical emission spectroscopy, sputter deposition

---

Abbreviations: GAS, gas aggregation cluster source; NP, nanoparticle; OES, optical emission spectroscopy; SEM, scanning electron microscopy; XPS, X-ray photoelectron spectroscopy.

1 | INTRODUCTION

Over the last few decades, metal nanoparticles (NPs) have attracted huge attention due to their unique properties resulting from the high surface-to-volume ratio. Their properties can be tuned by size distribution, filling factors, and surrounding media (e.g., in the case of nanocomposites), which makes them applicable in many fields like catalysis,[1] photocatalysis,[2–6] optics,[7] resistive switching,[8–15] and sensors.[16–20] In particular, noble metal alloy NPs with the composition as an additional tunable parameter are nowadays in the focus of researchers in a broad variety of application scenarios. Due to the unique properties of alloy noble metal NPs, especially of AgAu metal NPs, they can be utilized for different applications, including heterogeneous catalysis (e.g., oxidant-free benzyl alcohol dehydrogenation),[21] in surface plasmon-enhanced photocatalysis,[22] in solar cells,[23] as a potential advanced ink for anticounterfeiting purposes,[24] and for achieving a stable Ag ion release.[25] The optical properties of noble metal alloy NPs are also well known,[26] which are strongly dependent on the shape, size, size distribution, and composition of the NPs. Compared with conventional single-element NPs, the composition of alloy NPs is an additional crucial parameter, which can be used to tailor their performance in the respective application scenario. In this study, we focus on AgAu NPs motivated by recent interest in plasmonic nanocomposites,[27,28] functional nanocomposites,[29] solar energy harvesting,[23] and memristive devices.[14,30]

Possible synthesis approaches for alloy NPs range from biological over chemical to physical pathways, with solution-based chemical synthesis being the most common approach.[31,32] Physical vapor deposition (PVD) excels in generating high-purity NPs and does not rely on the utilization of surfactants. A broad variety of PVD-based strategies to produce alloy NPs with control over NP composition has already been employed successfully. These PVD strategies include surface energy-related self-organization of NPs on solid substrates[25,33–35] and in liquids (i.e., "Sputter into liquids")[36–38] as well as gas-phase synthesis. In this study, alloy AgAu NPs are fabricated using a PVD approach known as gas aggregation cluster source (GAS), which was first realized by Haberland in 1992.[39] In such a GAS, the NP sizes and size distributions are controlled by the magnetron power, gas flow, pressure, and aggregation length.[40] To produce alloy NPs inside such a GAS, three different ways are possible: the multiple magnetron approach,[40–44] the single-alloy target approach,[45–47] and the multicomponent target approach.[48]

Recent approaches with multiple magnetrons in a single GAS apparatus have enabled good control over NP composition, but this approach is costly, needs huge source dimensions, and is experimentally challenging, because interferences between individual magnetrons make the plasma control sometimes difficult.[40–44] Nevertheless, this method also allows control over the structure, for example, core–shell, core–shell–shell, and so forth. However, it can be sometimes challenging to achieve only alloy particles without core–shell particles, because the magnetrons are separated from each other. Using only one alloy target is also a suitable and simple strategy to synthesize alloy NPs, but controlled adjustment of alloy composition is not possible here.[45–47]

In a previous work, single magnetron sputtering inside a Haberland-type GAS with multicomponent targets was introduced as a new method to produce NPs with defined size distribution, high purity, and variable composition, which can be adjusted by the operating pressure in the GAS. In this method, one component is located in the erosion zone of an otherwise pure target, which serves as the second component. A change in pressure impacts the mean free path of Ar ions and, in turn, also influences the size of the erosion zone, which changes in the last consequence, due to the special target geometry, the composition of the produced NPs.[48]

Despite this simple relation between operating pressure and NP composition,[48] additional effects have to be considered for long-term depositions. It is known that in a GAS, a significant amount of material can be redeposited on the target surface,[49,50] which in the case of a multicomponent target may impact the alloy composition of the NPs. Furthermore, the erosion profile of the target can affect the NPs synthesis in a GAS.[51]

The deposition characteristics of the gas-phase synthesis of NPs, in general, are varying throughout the target lifetime,[49–51] which, in particular, is a challenge to be overcome in the case of multicomponent targets. Thus, a reliable in operando diagnostic approach is in high demand to satisfy the necessity of a precise control of the NP composition. In operando approaches are extremely useful to gain an insight into the NP formation process in a GAS, as the finally deposited NPs do not contain full information about any intermediate stages in the gas-phase synthesis. To analyze the growth and transport of NPs in the GAS, several in situ diagnostics, like small-angle X-ray scattering,[50,52] passive thermal probe, Langmuir probe,[53] and UV–Vis spectroscopy,[49] have already been applied successfully. In earlier reports, optical emission spectra (OES) were also successfully utilized to analyze sputter processes[54–56] or to analyze the oxidation and cluster formation processes in the GAS.[57]

In this study, the concept of alloy NP deposition by single-target sputtering from a multicomponent target is pursued. Special attention is being paid to the impact of target aging on the composition of AgAu NPs, and a

potential approach for in operando control of the NP composition is discussed. In the context of target aging, this study reveals that for the long-term use of multi-component targets inside a GAS, the composition of alloy NPs is gradually changing toward an enrichment in Au with each subsequent deposition cycle, which could be successfully attributed to redeposition effects. Redeposition is well known for magnetron sputtering. In the general picture, sputtered atoms may be redirected and adsorbed on the target surface due to collisions with gas atoms. The effect of redeposition is especially prominent in a GAS with its typical operational pressure range around 100 Pa, which is significantly higher as compared with conventional sputter deposition.[49,50,58,59] Whereas in the case of single-component targets, any redeposition solely changes the target's morphology and has no influence on elemental composition, in the case of alloy targets or multicomponent targets, local changes in composition have also to be considered. Redeposition is well known for pure single-component targets as well as in a GAS.[49,50] Furthermore, the target erosion profile influences the NPs synthesis and limits the working window in which NPs can be produced.[51] Due to these target history effects, a precise prediction of NP composition just based on operation pressure, which was suggested in an earlier report,[48] is impossible for long-term use of a multicomponent target. To account for the immense significance of precise control over NP properties for application purposes, a diagnostic approach to control the NP composition is presented. This approach goes beyond the application of OES as a tool for analysis of discharge characteristics[54–56] and utilizes a simple UV–Vis setup to record the OES of Ag and Au from the plasma. In this respect, in operando UV–Vis offers the possibility to record OES as well as obtain information on the NP plasmon resonance (PPR) of the NPs. Although the PPR is a great tool to obtain information about the growth and transport of NPs in the GAS (cf. transmission spectra of pure Ag and AgAu NPs in Figures S1 and S2), in this study, OES is presented as an efficient diagnostic tool to determine the composition of AgAu NPs in operando, which has the prospect to be used in future also for active control over the composition by the implementation of a feedback loop.

2 | EXPERIMENTAL SECTION

2.1 | Fabrication of the custom-build multicomponent target

The composite AgAu target was prepared by milling a radially symmetric trench of 3-mm width at the center of the erosion zone of an Ag target (99.99%, 2-inch diameter; Kurt J. Lesker). Three concentric rings of Au wire (99.95%, 1-mm diameter; Alfa Aesar) were put into the trench and embossed into the target. The chosen geometry allows a more effective use of the more costly Au.

2.2 | Deposition and analysis of NPs

The GAS with the deposition chamber was mounted on the transfer chamber of an Omicron XPS system (Omicron full lab). This configuration allows the transfer of the samples to the X-ray photoelectron spectroscopy (XPS) analytical chamber without exposure to air. The base pressure of the deposition chamber was 1.6×10^{-5} Pa, pumped by a turbomolecular pump (TMU 262; Pfeiffer Vacuum) and a scroll pump (Edwards 6i). The GAS was equipped with a 2″ height-adjustable and water-cooled DC magnetron (IX2U_9A327-02; Thin Films Consulting). The height-adjustable magnetron enables to tune the distance between the magnetron and the orifice of the GAS. This distance was kept constant and was only once adjusted, depending on the UV–Vis light beam, which is explained in Section 2.3. The deposition was performed at a DC power of 100 W, and the pressure inside the GAS was randomized for each deposition in a range between 37 and 188 Pa, corresponding to argon flows of 20 and 120 sccm, respectively. MDX 500 from Advanced Energy was used as a power supply and an Apex flow controller (AX-MC-200sccm-D/5M) with 200-sccm range was used for the gas flow regulation. The deposition time was adjusted individually for all samples, because different flows and pressures in the GAS change the deposition rate strongly. The time was set in a way that the surface coverage with NPs was sufficient to obtain reliable XPS spectra. The XPS spectra were evaluated with the software "CasaXPS." Each spectrum was analyzed by four different persons to reduce statistical and systematic errors that could occur, for example, during the background correction of an XPS spectrum. By that approach, we obtained a mean value for the NP composition. The highest and lowest calculated fractions were used as the error of the XPS measurements. Quartz wafers (0.5-mm thickness; Plan Optik) cut into 10×10 mm pieces were used as substrate material. Quartz was chosen, because it would allow ex situ UV–Vis transmission measurements to determine the optical properties. Depending on the selected operating pressure, the resulting NP diameters range from 2 to 30 nm (cf. scanning electron microscopy [SEM] micrographs in Figure S3 and the corresponding histograms of NP diameters in Figure S4).

2.3 | Measurement of OES

As the magnetron was height-adjustable, but the position of the access windows for the UV–Vis was fixed, the height of the magnetron was adjusted in a way that the UV–Vis light beam was in the closest distance to the magnetron without getting cut by the magnetron (Figure S5). The diameter of the light beam was 1.4 cm, and hence the distance between the center of the light beam and the ground cap of the magnetron was 0.7 cm. This position was fixed for all experiments to maintain the same aggregation length for the NPs. The integration time of the Ocean Optics spectrometer (STS-UV) was set to 25 ms and 40 spectra were averaged, so that every second, one spectrum was collected. After the background was subtracted from the counts, the height of the Ag I (328 nm) and Au I (312 nm) peaks was measured and averaged over the deposition time. The error of the spectrometer is small and can be neglected in comparison to the strong changes of the emission line spectrum induced by experimental parameters like, for example, pressure changes. A suitable error calculation was not possible, because any changes detected could be caused by a variation of an experimental parameter (e.g., change in sputter trench), and should be thus considered as a real signal.
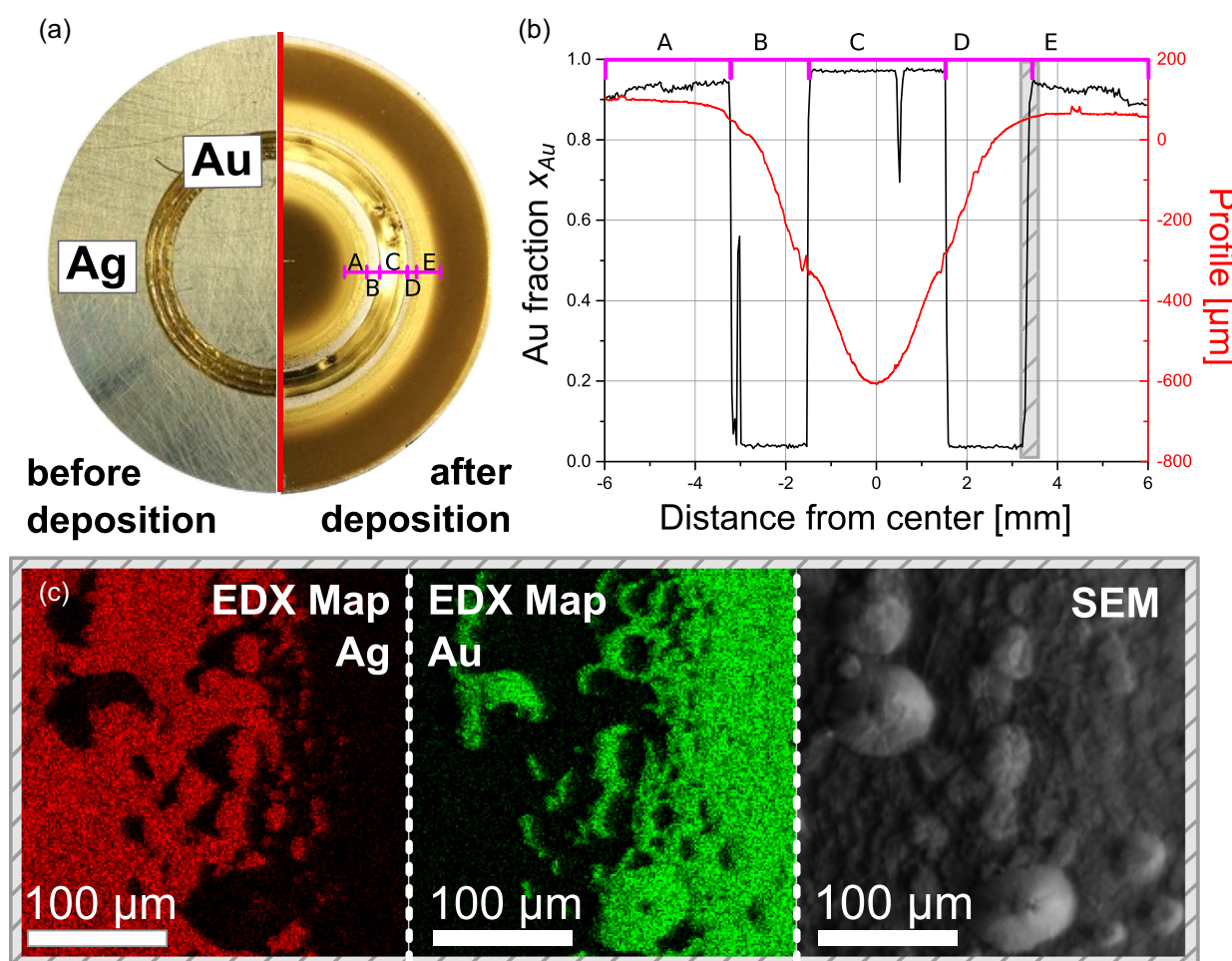
FIGURE 1 (a) A photograph of the target before (left) and after hours of deposition (right). The target surface is clearly enriched with Au after deposition. (b) The EDX line scan and depth profile of the target, as recorded after prolonged deposition, shows a clear transition between the Au wire and Ag target, but also an abrupt transition between the pure Ag target surface and the redeposition area, where the target surface is enriched by Au. The profile is in good agreement with the EDX line scan and shows that the transition region from the erosion zone to the redeposition zone lies exactly at the transition between Ag-rich region and Au-rich region. Here, the racetrack (sputter trench) includes the regions B, C, and D, where the center region (C) corresponds to the position of the embossed Au wires. The outer regions (A and E) correspond to the redeposition area. (c) The EDX map of the transition area between regions D (left) and E (right) shows a sharp transition between almost pure Ag (marked red) and Au (marked green). EDX, energy-dispersive X-ray spectroscopy; SEM, scanning electron microscopy

3 | RESULTS AND DISCUSSION

Within this section, it will be discussed that in the context of multicomponent targets with concentric rings at the center of the erosion zone, the redeposition adds another layer of complexity to a reliable determination of alloy NP composition.

In Figure 1a, a photographic image of an AgAu multicomponent target before (left half) and after prolonged deposition (right half) is shown. Whereas in the pristine state before deposition, the Au wires are embedded into a pure Ag target with a seemingly homogenous surface, after the prolonged deposition, two phenomena can be observed. The racetrack (erosion zone) of the target ranges over the Au wires (region C) and the adjacent regions (B and D). The remaining surface of the target is covered by redeposition of golden and dark golden color. To describe this redeposition effect in more detail, SEM energy-dispersive X-ray spectroscopy (EDX) measurements were performed, and the resulting EDX line profile of a scan over the regions A to E and the depth profile of the target (recorded via profilometry) are depicted in Figure 1b. The line scan shows that the target surface within regions A and E is Au-rich with an Au content of 90 at% and above. Before the deposition, these areas correspond to the pristine Ag target surface. Accordingly, the presence of the high Au content after the deposition indicates that in these areas, there is significant redeposition. The profilometer depth profile implies that the thickness of the deposit within areas A and E is roughly in the order of 64–100 μm. At the center of the erosion zone, in area C,

there is another Au-rich region, which corresponds to the embedded Au wires. Adjacent to the wires, areas B and D represent a region of almost pure Ag (Ag content 95 at% and above). There is a sharp transition from the Au-rich region C to the Ag-rich regions B and D, which is expected from the target geometry of the manufactured target before deposition. Interestingly, the transition between the regions A to B and D to E also appears very sharp and narrow in the EDX line scan. This observation indicates that there is a distinct boundary between the regions of redeposition (A and E) and the erosion zone (B–D). To gain further insights into this boundary, EDX elemental maps showing the Ag (red) and Au (green) content, as well as the corresponding SEM micrograph, are shown in Figure 1c. These measurements were obtained at the interface between regions D and E (as schematically depicted by a grey box in Figure 1b). The EDX maps underline that there is a sharp transition between the Au-rich redeposition region and the Ag-rich part of the erosion zone. In between the Ag-rich erosion zone (left, red) and the Au-rich redeposition zone (right, green), there is an overlap area with a width in the range of 100 μm. Within the overlap area, there are Au-rich and Ag-rich subregions; however, alloy-like smooth transitions are not observed.

To obtain additional information on the redeposition and target surface enrichment with Au, the target surface morphology was investigated by SEM (Figure 2). Besides the target surface Au enrichment effects, the surface morphology also varies across the different areas on the target. Whereas within the erosion zone (regions 3–6),
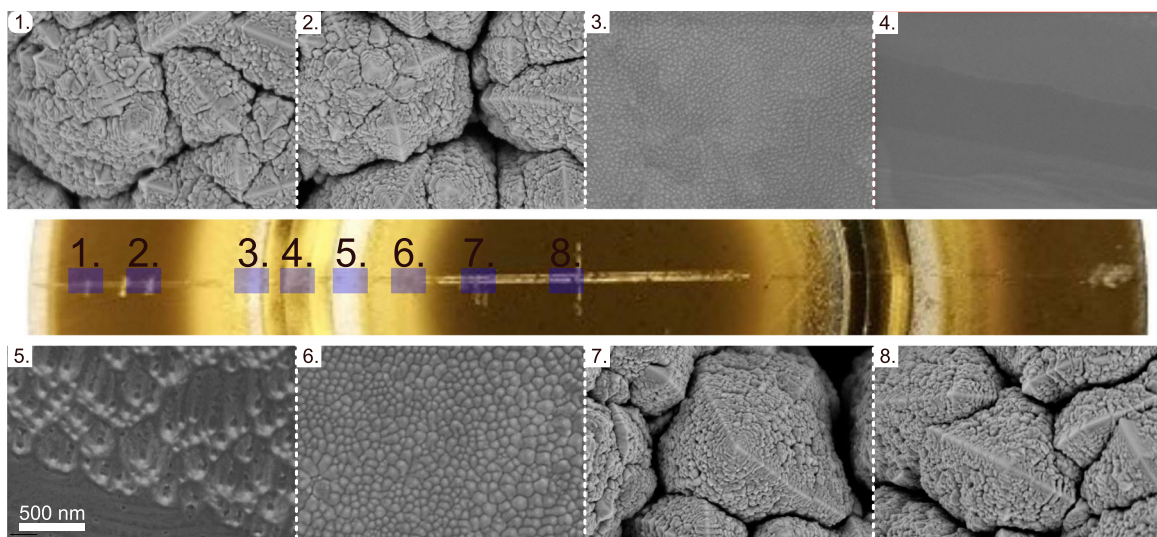

FIGURE 2 Scanning electron microscopy pictures from different positions on the target at the same magnification. The inset numbers show the position on the target from which the pictures are taken. Panels (1 and 2) and (7 and 8) show an interesting pyramid-like structure formed by the redeposition. For regions 3–6, the morphology is smooth and the surface exhibits spherical dome-like structures with a regular distribution

the morphology is smooth and the surface exhibits spherical dome-like structures with a regular distribution, the surface morphology at the redeposited areas is dominated by large, irregular structures with a high number of cracks in between (regions 1–2 and 7–8).

So far, the investigations on the target after prolonged deposition have shown that there is an abrupt transition between the Au-rich redeposition area and the Ag-rich part of the erosion zone. In fact, only within a small region (100-μm width as compared with 6.7-mm width for the overall erosion zone), an overlap of Au-rich and Ag-rich compartments has been observed. However, in the multicomponent target approach, the capability to control NP composition traces back to changes in the width of the effective erosion zone upon variation of pressure. This suggests that redeposition and target history will also impact the composition range, which can be achieved with the multicomponent target approach. In the following section, the effect of target history on the composition of AgAu NPs will be discussed. Within the range of the experimental aggregation pressure between 37 and 188 Pa, AgAu NPs with a gold fraction (xAu) between 54 and 82 at% were obtained. More deposition details can be found in Section 2.2. The results from a quantification of the Au fraction based on the Au 4d and Ag 3d lines (cf. Figure S6) from the recorded XPS spectra are shown in Figure 3a, where the Au fraction is plotted versus the pressure in the GAS. The plot shows that the linear relation between alloy NPs composition and operating pressure, which was proposed in an earlier work, is not completely sufficient to describe the composition

dependence of the AgAu NPs, which is reflected in a rather low linear correlation coefficient of 0.833 (Pearson correlation).[48] In contrast to the first study by Vahl et al.,[48] the deposition times were increased drastically and a higher number of individual depositions were investigated. This implies that changes on the target surface due to redeposition also impact the composition of alloy NPs from multicomponent targets in a GAS. To also account for the effect of target aging in terms of redeposition, we incorporated the accumulated deposition time as a measure of target history as a second parameter into a linear regression. Hence, the target history is defined as the sum of all individual deposition times of the experiments as well as the preparation times, where the discharge was on but the shutter was closed. Using a linear fit with pressure and target history as parameters, the fit (blue line) is in reasonable agreement (correlation coefficient of 0.983) with the composition data from XPS quantification (red bars), as depicted in Figure 3b.

For practical applications, the parameter of target history is not very useful, as it is not obtainable in the experiment itself but only accessible via bookkeeping over every experiment's deposition time. An in operando diagnostic approach, which is capable of directly determining the NPs composition, is highly favorable. Such an approach could also be used to control the NPs composition via a feedback loop, for example, controlling the gas flow. In the following section, in operando optical spectroscopy techniques are discussed as a potential pathway to enable control over NP composition.
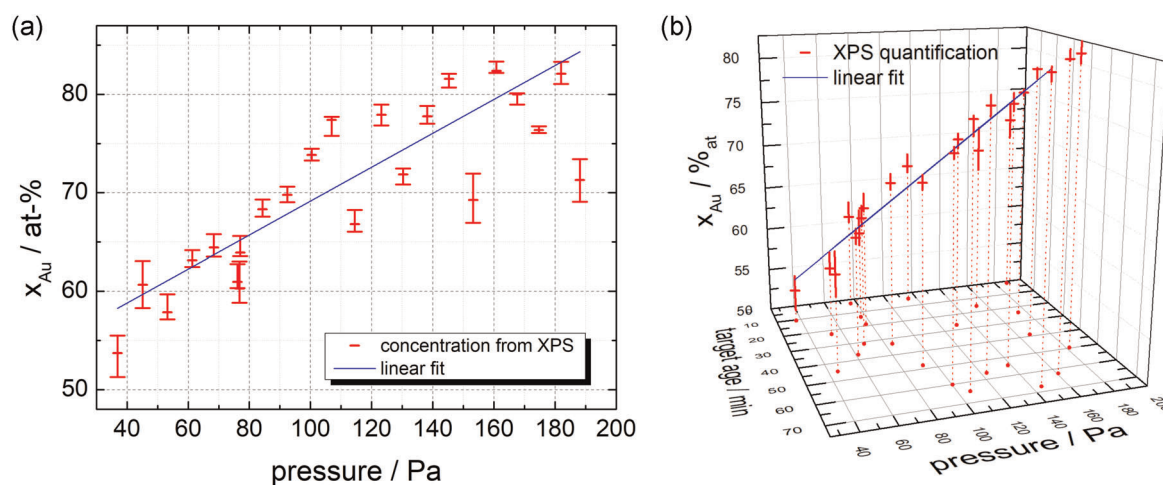

FIGURE 3 Evaluation of the Au fractions of AgAu NPs (xAu) as experimentally obtained from X-ray photoelectron spectroscopy (XPS) quantification. The plot of gold fractions versus operating pressure (a) shows a considerable deviation from the expected simple linear behavior (Pearson correlation coefficient: 0.833),[41] which indicates that additional parameters impact the resulting composition of the nanoparticles. In this context, the target lifetime (i.e., the cumulative deposition time) correlates with the ongoing change in redeposition. In the 3D plot of the gold fraction versus target lifetime as well as pressure (b), the linear fit shows a reasonable agreement (Pearson correlation coefficient: 0.983)

Considering the plasmonic properties of noble metal (alloy) NPs, such as AgAu, an in operando monitoring of the plasmon absorption peak by UV–Vis spectroscopy can be applied to obtain information about the NPs.[49] However, this approach renders very challenging for alloy NPs, due to the extinction coefficient as well as the simultaneous influence of NPs diameter and composition on the plasmon peak's wavelength (Figures S1 and S2).[60,61] However, by using the identical UV–Vis setup also, direct optical emission lines (OES) from the Ag and Au species in the plasma can be recorded, which consequently makes OES a viable diagnostic approach to be used complementary to in situ UV–Vis. OES has already been reported as a tool to monitor compositional changes of thin films in conventional sputter deposition processes.[54–56,62] The intensity in an OES spectrum is related to the amount of excited atoms of a specific element in the gas phase, and a good correlation between the intensity of optical emission lines and the resulting elemental concentrations in thin films is commonly reported.[54–56,62] Although in a conventional sputter deposition process, all sputtered atoms that enter the gas phase are contributing to the thin film, the formation of alloy NPs in a gas-phase synthesis adds another layer of complexity. One cannot be sure whether all sputtered atoms of both elements are contributing equally to the formation of NPs. One possibility is that one element preferentially contributes to the cluster growth and more of the other elements get lost on the walls of the GAS. Nevertheless, the intensity of an emission line for a specific element is related to the concentration of this element in the plasma and should correlate with the fraction of this element in the formed NPs. One advantage of using OES is also that different sputter yields of the individual components of the multicomponent

target do not play a role, because only already sputtered atoms can contribute to the signal. An exemplary OES spectrum, recorded in operando during a typical alloy NP deposition, is shown in Figure 4a. Within the range from 305 to 345 nm, three optical emission lines corresponding to the elements Ag (indicated by orange color) and Au (indicated by blue color) are observed. We assign the line around 312 nm to the Au I emission line at 312.28 nm and the line around 327 nm to Ag I line at 328.07 nm. These are the most intense lines with the shortest wavelength difference to each other for each element within this range. Both the Au I line at 312 nm and the Ag I line at 328 nm were intense enough to record them over the whole pressure range studied in this study. For further evaluations, the peak intensities of these lines, $I_{Ag\,I}$ and $I_{Au\,I}$, were extracted from the spectra.

To underline the effect of redeposition and target aging, we investigated the time evolution of the selected Au I and Ag I emission lines. For this purpose, at first, the target was conditioned by running a deposition at a pressure of 168 Pa, which corresponds to a narrow sputter region (i.e., narrow erosion zone) and yields considerable redeposition. The following deposition is operated at a significantly lower pressure of 45 Pa, which results in a broader sputter region that also covers a part of the redeposited area. In Figure 4b, the time evolution of the peak intensities $I_{Ag\,I}$ and $I_{Au\,I}$ during the deposition at a pressure of 45 Pa is shown. During the deposition, $I_{Ag\,I}$ is increasing, whereas $I_{Au\,I}$ is decreasing simultaneously. This change is especially prominent within the initial period of the deposition (with time constant $\tau \sim 47.9$ s) and settles gradually within the final period of the deposition. A similar behavior is observed regularly, if the pressure decreases drastically in comparison to the previous deposition. This is in good
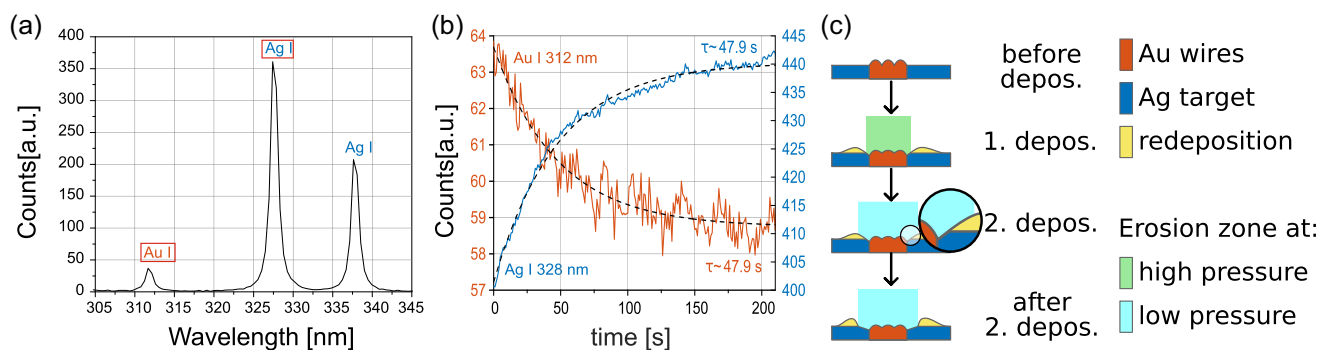
FIGURE 4 Exemplary optical emission spectroscopy during the deposition of AgAu nanoparticles. (a) The peaks in the spectrum can be clearly attributed to the emission lines of the elements Ag (indicated by blue color) and Au (orange), and the two emission lines that are considered for further evaluations are marked with a red rectangle. These two emission lines were selected for further evaluations due to their high intensity as well as a small difference in wavelength. (b) Time evolution of the Au I and Ag I emission lines for an exemplary deposition after a drastic pressure reduction from 168 to 45 Pa. Au I exhibits an exponential decay in the peak intensity over deposition time. This behavior is an effect of target history caused by redeposition, which is schematically sketched in (c)

agreement with our EDX analysis of the target after the deposition, which showed an abrupt change between Au- and Ag-rich regions. The effect of target history and re-deposition is schematically depicted in Figure 4c in terms of the time evolution of the target cross-section. For high pressures, the erosion zone is narrow (indicated in green in Figure 4c) and a lot of Au is redeposited on the target in the vicinity of the erosion zone (indicated in yellow). If in the next deposition, the pressure during the deposition is reduced, the erosion zone will be wider (cyan color) and also a lot of the redeposited material (AgAu) will be sputtered off until the redeposited material is removed from the erosion zone. However, when the target is conditioned by running a deposition at a pressure of 92.4 Pa, this corresponds to a broader sputter region. When afterward the pressure is increased to 182 Pa, which corresponds to a narrow sputter region, nearly no changes in the emission lines over time are visible, because no redeposited material gets sputtered (Figure S7). Before each deposition of NPs, the target was cleaned and conditioned by running the discharge for 60 s, because earlier experiments have shown that this time is sufficient to clean the target and to obtain a stable cluster formation and deposition rate. The cleaning was performed with a closed shutter at the pressure under which the following deposition should be performed, so that no clusters can approach the substrate. However, the effect of target history on the resulting NP composition (Figure 3), as well as the gradual change in $I_{Ag\,I}$ and $I_{Au\,I}$, as observed by OES, indicates that the pre-deposition cleaning time was too short to reduce the effect of re-deposition and the target got gradually enriched with Au. Nevertheless, also the change in the target geometry over the lifetime due to erosion can possibly influence the composition slightly. The effect of target erosion could not be overcome by longer cleaning times, but the effect of redeposition plays a major role.

However, as OES is able to capture the change of the peak intensities I_{Ag} and I_{Au} in operando, we will elaborate in the following section how OES can be applied as a diagnostic tool to determine the NP composition. In the most general approximation, the peak intensities of the most intensive emission lines for the elements Ag and Au are related to the presence of excited Ag and Au species in the plasma. The amount of excited Ag and Au species in the plasma, in turn, is related to the overall amount of sputtered species from the target. On the basis of the assumption that the NPs form via nucleation, growth, and coalescence from Ag and Au atoms from the gas phase, the composition (in terms of the atomic fraction of Au, x_{Au} in atomic percent) of the resulting NPs can be expressed by Equation (1).

$$x_{Au} \propto \frac{c_{Au} \times \overline{I_{Au\,I}}}{c_{Au} \times \overline{I_{Au\,I}} + c_{Ag} \times \overline{I_{Ag\,I}}}, \tag{1}$$

$$\frac{1}{x_{Au}} - 1 \propto c_{rel} \times \frac{\overline{I_{Ag\,I}}}{\overline{I_{Au\,I}}}; \; c_{rel} = \frac{c_{Ag}}{c_{Au}}, \tag{2}$$

$$c_{rel} = (c_1 \times p) + c_2, \tag{3}$$

$$\frac{1}{x_{Au}} - 1 \propto c_1 \times p \times \frac{\overline{I_{Ag\,I}}}{\overline{I_{Au\,I}}} + c_2 \times \frac{\overline{I_{Ag\,I}}}{\overline{I_{Au\,I}}}. \tag{4}$$

Here, the values of peak intensities of the selected emission lines I_{Au} and I_{Ag}, averaged over the whole deposition time, are representing the amount of excited Au and Ag species in the plasma. Furthermore, coefficients c_{Au} and c_{Ag} are introduced to take into account the potential differences in the contributions of Ag and Au to the OES signal and to the NP composition. Therefore, the intensity coefficients cover two aspects: On the one hand, the fraction of excited species for Au and Ag depends on the plasma parameters and, on the other hand, the growth process of NPs in the gas-phase synthesis may lead to a different incorporation of Ag and Au into the NPs.

Instead of considering separate intensity coefficients c_{Au} and c_{Ag}, Equation (1) can be simplified by using a relative intensity coefficient c_{rel} (Equation 2).

The plot of $(1/x_{Au}) - 1$ versus $\overline{I_{Ag\,I}}/\overline{I_{Au\,I}}$ in Figure 5a shows a nonlinear relation, which implies that the coefficient c_{rel} is not readily described by a constant. In contrast, the color scale in Figure 5a indicates that the pressure does impact coefficient c_{rel}. In this context, it is important to mention that with varying pressure inside the GAS, the position and width of the plasma zone are also varying. In addition, the variation of pressure also impacts plasma parameters like electron energy distribution function and electron density. To accommodate any potential effect of pressure, the fitting parameter c_{rel} can be written in a linear approximation (Equation 3), which is used in the following evaluation. Inserting Equation (3) into Equation (2), the empirical fit model is obtained, as shown in Equation (4).

To test the derived fit model, the first four depositions (blue color, calibration) were used to obtain the fit parameters c_1 and c_2. In the experiment, the parameters for the first four depositions were selected, such that the full pressure range from approximately 37 to 188 Pa is covered. Using these fit parameters as well as the diagnostic quantities pressure p and OES intensities, as shown in Figure 5b, the NP composition can be estimated for the following 19 depositions (red color, test). The fitted NP composition $x_{Au,\,fit}$ correlates well with the experimentally determined NP composition $x_{Au,\,XPS}$. The
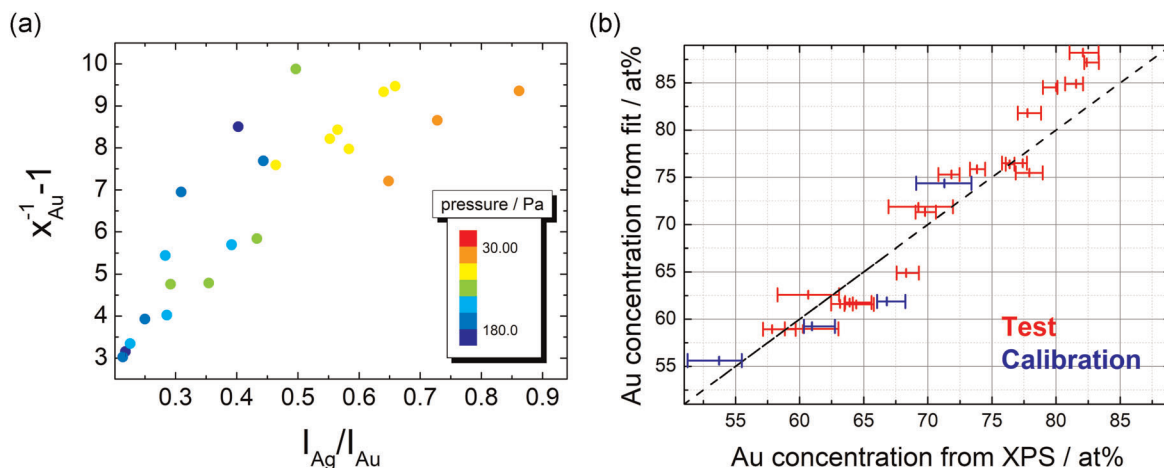
FIGURE 5 The plot of $(1/x_{Au}) - 1$ versus $\overline{I_{AgI}}/\overline{I_{AuI}}$ in (a) shows a nonlinear relation and indicates that coefficient c_{rel} is not readily described by a constant. The color scale implies that the pressure does impact coefficient c_{rel}. (b) The intensities obtained from in operando optical emission spectroscopy (OES), as well as the operating pressure, are taken into account (Equation 4) from the first four depositions (blue color, calibration). Afterward, the Au fraction can be reasonably predicted for the following 19 depositions only by measuring OES and pressure (red color, test)

correlation factor (0.970) is very close to the earlier evaluation under application of the target history (0.983), as depicted in Figure 3. However, compared with the target history, the intensity ratio and the operating pressure are easily obtainable by diagnostic approaches, in operando at each timestep of the NP deposition. Thus, OES proved to be a valuable tool to determine the composition of alloy NPs inside a GAS, as soon as a series of reference NP depositions has been analyzed regarding its composition and the fitting parameters have been determined according to the empirical relation described in Equation (4). Within its tested validity range (I_{Ag}/I_{Au} between 3.03 and 9.87; p between 37 and 188 Pa), which is given by the set of AgAu NPs that have been investigated by XPS quantification, the empirical model offers a good estimate of the composition of the AgAu NPs that are just formed at these conditions. The effect of redeposition and target aging, while altering the range of obtainable NP compositions over the lifetime of the target, is here already reasonably covered by the changes in the intensity ratio. After the determination of the fitting parameters, the presented method yields a good basis for in operando control over the alloy composition of NPs.

4 | CONCLUSION

In this study, the gas-phase synthesis via a gas aggregation source with a multicomponent target was applied to fabricate AgAu alloy NPs with an Au fraction ranging from 54 to 82 at%. In this study, on the one hand, the effect of redeposition on the composition of alloy NPs is

discussed. It is shown that the multicomponent target was enriched with gold over the course of experiments due to redeposition. The phenomenon of redeposition is well known for pure metallic NP production in a GAS and is related to the higher pressures in comparison to normal sputter deposition. During the compositional analysis of the NPs, we were able to show that composition does not only depend on the pressure in the GAS but also on the cumulative deposition time. The relation between target lifetime and composition is attributed to the gold enrichment of the target due to redeposition. A linear fit incorporating operating pressure and target history (cumulative deposition time) was found to capture the obtained NP compositions well. On the other hand, a versatile and robust approach for in operando diagnostics is presented. It was demonstrated that for practical applications, an in operando diagnostic approach is highly favorable over using a fitting function based on cumulative deposition time, which is not an intrinsic property of the target. Therefore, we searched for an in operando diagnostic approach, which is able to solve the problem of the target aging. A versatile, robust, and simple diagnostic approach is described by using in operando OES. A good correlation between operating pressure, intensity ratio of Ag and Au emission lines, and the experimentally obtained NP compositions was found. With the addition of in operando OES, it is possible to determine the alloy NPs fraction for a broad variety of alloy systems, which are deposited by a GAS based on magnetron sputtering using the multicomponent target approach. In future, an in operando feedback loop could be implemented, which can measure the pressure and

the OES to operate the flow controller in operando according to the composition needs of the operator.

CONFLICT OF INTERESTS

The authors declare that there are no conflict of interests.

AUTHOR CONTRIBUTIONS

Jonas Drewes, Alexander Vahl, Oleksandr Polonsky, Thomas Strunskus, and Franz Faupel developed the idea and conceived the initial design of the study. Jonas Drewes, Oleksandr Polonsky, and Alexander Vahl established the experimental setup around the multi-component target approach. Jonas Drewes performed the AgAu NP depositions and recorded XPS and UV–Vis data. Jonas Drewes, Alexander Vahl, Oleksandr Polonsky, and Niko Carstens analyzed the results, including XPS quantification. Alexander Vahl, Jonas Drewes, and Niko Carstens elaborated the multiple regression model and performed correlation analysis. Jonas Drewes and Alexander Vahl prepared the manuscript draft. Franz Faupel supervised the work of Jonas Drewes, Alexander Vahl, and Niko Carstens. All authors have discussed the experimental results and their analysis and revised and approved the manuscript.

DATA AVAILABILITY STATEMENT

The XPS and UV–Vis spectra that support the findings of this study are available from the corresponding author upon reasonable request.

ORCID

Jonas Drewes https://orcid.org/0000-0002-8539-1543
Alexander Vahl https://orcid.org/0000-0002-7311-272X
Thomas Strunskus https://orcid.org/0000-0003-3931-5635
Oleksandr Polonskyi https://orcid.org/0000-0001-5013-0944
Franz Faupel https://orcid.org/0000-0003-3367-1655

REFERENCES

[1] D. Astruc, *Chem. Rev.* **2020**, *120*, 461.
[2] M. Z. Ghori, S. Veziroglu, A. Hinz, B. B. Shurtleff, O. Polonskyi, T. Strunskus, J. Adam, F. Faupel, O. C. Aktas, *Nano Mater.* **2018**, *1*, 3760.
[3] S. Veziroglu, M. Z. Ghori, A. L. Obermann, K. Röder, O. Polonskyi, T. Strunskus, F. Faupel, O. C. Aktas, *Mater. Sci.* **2019**, *216*, 1.
[4] S. Veziroglu, J. Hwang, J. Drewes, I. Barg, J. Shondo, T. Strunskus, O. Polonskyi, F. Faupel, O. C. Aktas, *Mater. Today Chem.* **2020**, *16*, 100251.
[5] A. Vahl, S. Veziroglu, B. Henkel, T. Strunskus, O. Polonskyi, O. C. Aktas, F. Faupel, *Materials (Basel)* **2019**, *12*, 2840.
[6] H. Li, Z. Li, Y. Yu, Y. Ma, W. Yang, F. Wang, X. Yin, X. Wang, *J. Phys. Chem. C* **2017**, *121*, 12071.
[7] C. Minnai, M. Di Vece, P. Milani, *Nanotechnology* **2017**, *28*, 355702.
[8] C. Minnai, A. Bellacicca, S. A. Brown, P. Milani, *Sci. Rep.* **2017**, *7*, 1.
[9] M. Mirigliano, D. Decastri, A. Pullia, D. Dellasega, A. Casu, A. Falqui, P. Milani, *Nanotechnology* **2020**, *31*, 234001.
[10] M. Mirigliano, F. Borghi, A. Podestà, A. Antidormi, L. Colombo, P. Milani, *Nanoscale Adv.* **2019**, *1*, 3119.
[11] Z. Wang, S. Joshi, S. E. Savel'ev, H. Jiang, R. Midya, P. Lin, M. Hu, N. Ge, J. P. Strachan, Z. Li, Q. Wu, M. Barnell, G. L. Li, H. L. Xin, R. S. Williams, Q. Xia, J. J. Yang, *Nat. Mater.* **2017**, *16*, 101.
[12] H. Jiang, D. Belkin, S. E. Savel'Ev, S. Lin, Z. Wang, Y. Li, S. Joshi, R. Midya, C. Li, M. Rao, M. Barnell, Q. Wu, J. J. Yang, Q. Xia, *Nat. Commun.* **2017**, *8*, 882.
[13] B. J. Choi, A. C. Torrezan, K. J. Norris, F. Miao, J. P. Strachan, M. X. Zhang, D. A. A. Ohlberg, N. P. Kobayashi, J. J. Yang, R. S. Williams, *Nano Lett.* **2013**, *13*, 3213.
[14] S. H. Jo, T. Chang, I. Ebong, B. B. Bhadviya, P. Mazumder, W. Lu, *Nano Lett.* **2010**, *10*, 1297.
[15] X. Yan, J. Zhao, S. Liu, Z. Zhou, Q. Liu, J. Chen, X. Y. Liu, *Adv. Funct. Mater.* **2018**, *28*, 1.
[16] V. Postica, A. Vahl, D. Santos-Carballal, T. Dankwort, L. Kienle, M. Hoppe, A. Cadi-Essadek, N. H. de Leeuw, M. I. Terasa, R. Adelung, F. Faupel, O. Lupan, *ACS Appl. Mater. Interfaces* **2019**, *11*, 31452.
[17] Y. Yong, C. Li, X. Li, T. Li, H. Cui, S. Lv, *J. Phys. Chem. C* **2015**, *119*, 7534.
[18] S. W. Choi, A. Katoch, G. J. Sun, S. S. Kim, *Sens. Actuators, B* **2013**, *181*, 446.
[19] F. Fan, J. Zhang, J. Li, N. Zhang, R. R. Hong, X. Deng, P. Tang, D. Li, *Sens. Actuators, B* **2017**, *241*, 895.
[20] K. Hassan, G. S. Chung, *Sens. Actuators, B* **2017**, *239*, 824.
[21] J. Zheng, J. Qu, H. Lin, Q. Zhang, X. Yuan, Y. Yang, Y. Yuan, *ACS Catal.* **2016**, *6*, 6662.
[22] W. Hou, S. B. Cronin, *Adv. Funct. Mater.* **2013**, *23*, 1612.
[23] M. A. Al-Azawi, N. Bidin, M. Bououdina, S. M. Mohammad, *Sol. Energy* **2016**, *126*, 93.
[24] J. P. Wilcoxon, P. P. Provencio, *J. Am. Chem. Soc.* **2004**, *126*, 6402.
[25] N. Alissawi, V. Zaporojtchenko, T. Strunskus, I. Kocabas, V. S. K. Chakravadhanula, L. Kienle, D. Garbe-Schönberg, F. Faupel, *Gold Bull.* **2013**, *46*, 3.
[26] R. Ferrando, J. Jellinek, R. L. Johnston, *Chem. Rev.* **2008**, *108*, 845.
[27] M. Elbahri, M. K. Hedayati, V. S. Kiran Chakravadhanula, M. Jamali, T. Strunskus, V. Zaporojtchenko, F. Faupel, *Adv. Mater.* **2011**, *23*, 1993.
[28] M. K. Hedayati, M. Javaherirahim, B. Mozooni, R. Abdelaziz, A. Tavassolizadeh, V. S. K. Chakravadhanula,

V. Zaporojtchenko, T. Strunkus, F. Faupel, M. Elbahri, *Adv. Mater.* **2011**, *23*, 5410.

[29] F. Faupel, V. Zaporojtchenko, T. Strunskus, M. Elbahri, *Adv. Eng. Mater.* **2010**, *12*, 1177.

[30] A. Vahl, N. Carstens, T. Strunskus, F. Faupel, A. Hassanien, *Sci. Rep.* **2019**, *9*, 1.

[31] X.-F. Zhang, Z.-G. Liu, W. Shen, S. Gurunathan, *Int. J. Mol. Sci.* **2016**, *17*, 1534.

[32] S. Gurunathan, K. Kalishwaralal, R. Vaidyanathan, D. Venkataraman, S. R. K. Pandian, J. Muniyandi, N. Hariharan, S. H. Eom, *Colloids Surf., B* **2009**, *74*, 328.

[33] M. Petr, O. Kylián, A. Kuzminova, J. Kratochvíl, I. Khalakhan, J. Hanuš, H. Biederman, *Opt. Mater. (Amst).* **2017**, *64*, 276.

[34] H. T. Beyene, V. S. K. Chakravadhanula, C. Hanisch, M. Elbahri, T. Strunskus, V. Zaporojtchenko, L. Kienle, F. Faupel, *J. Mater. Sci.* **2010**, *45*, 5865.

[35] M. Gensch, M. Schwartzkopf, W. Ohm, C. J. Brett, P. Pandit, S. K. Vayalil, L. Bießmann, L. P. Kreuzer, J. Drewes, O. Polonskyi, T. Strunskus, F. Faupel, A. Stierle, P. Müller-Buschbaum, S. V. Roth, *ACS Appl. Mater. Interfaces* **2019**, *11*, 29416.

[36] M. T. Nguyen, T. Yonezawa, *Sci. Technol. Adv. Mater.* **2018**, *19*, 883.

[37] M. T. Nguyen, T. Yonezawa, Y. Wang, T. Tokunaga, *Mater. Lett.* **2016**, *171*, 75.

[38] M. Meischein, M. Fork, A. Ludwig, *Nanomaterials* **2020**, *10*, 20.

[39] H. Haberland, M. Karrais, M. Mall, Y. Thurner, *J. Vac. Sci. Technol., A* **1992**, *10*, 3266.

[40] Y. Huttel, L. Martínez, A. Mayoral, I. Fernández, *MRS Commun.* **2019**, *8*, 947.

[41] P. Grammatikopoulos, S. Steinhauer, J. Vernieres, V. Singh, M. Sowwan, *Adv. Phys. X* **2016**, *1*, 81.

[42] P. Solař, J. Hanuš, M. Cieslar, T. Košutová, K. Škorvánková, O. Kylián, P. Kúš, H. Biederman, *J. Phys. D: Appl. Phys.* **2020**, *53*, 195303.

[43] Y. Huttel, *Gas-Phase Synthesis of Nanoparticles*, 1st ed., Wiley-VCH Verlag GmbH & Co. KGaA, Weinheim **2017**, p. 79.

[44] L. Martínez, M. Díaz, E. Román, M. Ruano, P. D. Llamosa, Y. Huttel, *Langmuir* **2012**, *28*, 11241.

[45] A. Mayoral, L. Martínez, J. M. García-Martín, I. Fernández-Martínez, M. García-Hernández, B. Galiana, C. Ballesteros, Y. Huttel, *Nanotechnology* **2018**, *30*, 065606.

[46] D. Llamosa Pérez, A. Espinosa, L. Martínez, E. Román, C. Ballesteros, A. Mayoral, M. García-Hernández, Y. Huttel, *J. Phys. Chem. C* **2013**, *117*, 3101.

[47] A. I. Ayesh, *J. Alloys Compd.* **2018**, *745*, 299.

[48] A. Vahl, J. Strobel, W. Reichstein, O. Polonskyi, T. Strunskus, L. Kienle, F. Faupel, *Nanotechnology* **2017**, *28*, 175703.

[49] D. Nikitin, J. Hanuš, S. Ali-Ogly, O. Polonskyi, J. Drewes, F. Faupel, H. Biederman, A. Choukourov, *Plasma. Processes Polym.* **2019**, *16*, 1.

[50] A. Shelemin, P. Pleskunov, J. Kousal, J. Drewes, J. Hanuš, S. Ali-Ogly, D. Nikitin, P. Solař, J. Kratochvíl, M. Vaidulych, M. Schwartzkopf, O. Kylián, O. Polonskyi, T. Strunskus, F. Faupel, S. V. Roth, H. Biederman, A. Choukourov, *Part. Part. Syst. Charact.* **2020**, *37*, 1.

[51] A. Rai, A. Mutzke, G. Bandelow, R. Schneider, M. Ganeva, A. V. Pipa, R. Hippler, *Nucl. Instrum. Methods Phys. Res., Sect. B* **2013**, *316*, 6.

[52] J. Kousal, A. Shelemin, M. Schwartzkopf, O. Polonskyi, J. Hanuš, P. Solař, M. Vaidulych, D. Nikitin, P. Pleskunov, Z. Krtouš, T. Strunskus, F. Faupel, S. V. Roth, H. Biederman, A. Choukourov, *Nanoscale* **2018**, *10*, 18275.

[53] S. Gauter, F. Haase, P. Solař, O. Kylián, P. Kúš, A. Choukourov, H. Biederman, H. Kersten, *J. Appl. Phys.* **2018**, *124*, 073301.

[54] A. Raveh, M. Weiss, R. Schneck, *Surf. Coat. Technol.* **1999**, *111*, 263.

[55] J. Posada, A. Bousquet, M. Jubault, D. Lincot, E. Tomasella, *Plasma Processes Polym.* **2016**, *13*, 997.

[56] S.-K. Wu, K.-H. Tseng, *Mater. Trans.* **2002**, *43*, 871.

[57] A. Shelemin, O. Kylián, J. Hanuš, A. Choukourov, I. Melnichuk, A. Serov, D. Slavínská, H. Biederman, *Vacuum* **2015**, *120*, 162.

[58] S. M. Rossnagel, I. Yang, J. J. Cuomo, *Thin Solid Films* **1991**, *199*, 59.

[59] D. Depla, *Nucl. Instrum. Methods Phys. Res., Sect. B* **2014**, *328*, 65.

[60] S. Enoch, B. Nicolas, A. Adibi, T. W. Hänsch, F. Krausz, B. A. J. Monemar, H. Venghaus, H. Weber, H. Weinfurter, *Plasmonics*, Vol. 167 (Eds: S. Enoch, N. Bonod), Springer, Berlin, Heidelberg **2012**.

[61] S. Link, Z. L. Wang, M. A. El-Sayed, *J. Phys. Chem. B* **1999**, *103*, 3529.

[62] S. Inoue, H. Uchida, A. Hioki, K. Koterazawa, R. P. Howson, *Thin Solid Films* **1995**, *271*, 15.

SUPPORTING INFORMATION

Additional Supporting Information may be found online in the supporting information tab for this article.